

MS FILE COPY

(3)

## PROPAGATION DIAGNOSTICS MEASUREMENTS

**Microwave Diagnostics of the ATA  
Electron Beam Propagating in Air.**

Final Technical Report

August 1988

By: K. R. Stalder, M. S. Williams, and D. J. Eckstrom

Sponsored By:

DEFENSE ADVANCED RESEARCH PROJECTS AGENCY  
1400 Wilson Blvd.  
Arlington, VA 22209-2308

Monitored by:

Naval Surface Warfare Center  
Silver Springs, MD 20910

ARPA Order No. 4395/54  
Contract No. N60921-85-C-0170  
Effective Date: 22 April 1985  
Expiration Date: 21 April 1988  
Principal Investigator: D. J. Eckstrom (415) 859-4398

SRI Project PYU-8606  
MP Report No. 88-213

DTIC  
SELECTED  
17 APR 1989  
S E D  
C E

The views and conclusions contained in this document are those of the authors and should not be interpreted as necessarily representing official policies, either expressed or implied, of the Defense Advanced Research Projects Agency or the U.S. Government.

SRI International  
333 Ravenswood Avenue  
Menlo Park, California 94025-3493  
(415) 326-6200  
TWX: 910-373-2046  
Telex: 334486



This document has been approved  
for public release and sales. The  
distribution is unlimited.

89 1000

Unclassified

SECURITY CLASSIFICATION OF THIS PAGE

Form Approved  
OMB No. 0704-0188

## REPORT DOCUMENTATION PAGE

1a. REPORT SECURITY CLASSIFICATION UNCLASSIFIED		1b. RESTRICTIVE MARKINGS None	
2a. SECURITY CLASSIFICATION AUTHORITY DARPA-CG-55		3. DISTRIBUTION/AVAILABILITY OF REPORT Approved for public release; distribution unlimited.	
2b. DECLASSIFICATION/DOWNGRADING SCHEDULE N/A			
4. PERFORMING ORGANIZATION REPORT NUMBER(S) MP 88-213		5. MONITORING ORGANIZATION REPORT NUMBER(S)	
6a. NAME OF PERFORMING ORGANIZATION SRI International	6b. OFFICE SYMBOL (If applicable)	7a. NAME OF MONITORING ORGANIZATION Naval Surface Warfare Center	
6c. ADDRESS (City, State, and ZIP Code) 333 Ravenswood Avenue Menlo Park, CA 94025		7b. ADDRESS (City, State, and ZIP Code) Silver Spring, MD 20910	
8a. NAME OF FUNDING/SPONSORING ORGANIZATION Defense Advanced Research Projects Agency	8b. OFFICE SYMBOL (If applicable)	9. PROCUREMENT INSTRUMENT IDENTIFICATION NUMBER Contract No. N60921-85-C-0170	
8c. ADDRESS (City, State, and ZIP Code) 1400 Wilson Boulevard Arlington, VA 22209		10. SOURCE OF FUNDING NUMBERS PROGRAM ELEMENT NO.      PROJECT NO.      TASK NO.      WORK UNIT ACCESSION NO.	
11. TITLE (Include Security Classification) PROPAGATION DIAGNOSTICS MEASUREMENTS. MICROWAVE DIAGNOSTICS OF THE ATA ELECTRON BEAM PROPAGATING IN AIR			
12. PERSONAL AUTHOR(S) K. R. Stalder, M. S. Williams, and D. J. Eckstrom			
13a. TYPE OF REPORT Final Technical	13b. TIME COVERED FROM 850422 TO 880421	14. DATE OF REPORT (Year, Month, Day) 1988 August 22	15. PAGE COUNT
16. SUPPLEMENTARY NOTATION			
17. COSATI CODES FIELD      GROUP      SUB-GROUP 20      09 20      07		18. SUBJECT TERMS (Continue on reverse if necessary and identify by block number) Electron Beams, conductivity, afterglows, microwave diagnostics, plasmas	
19. ABSTRACT (Continue on reverse if necessary and identify by block number)  Experiments on conductivity profiling around a propagating electron beam were successfully performed during the Spring 1987 series of open-air propagation experiments on ATA at LLNL. Our measurements consisted of both 10- and 35-GHz microwave interferometer measurements of real and imaginary conductivity histories along chords at various y-offsets from the beam centerline and at two different locations along the propagating beam line.  The 35-GHz probe beam, located near the beam exit foil at the end of the closed beamline, was totally attenuated during the electron beam pulse for the total range of the measurements from y = -4 cm to y = +12 cm. Theoretical calculations indicate			
20. DISTRIBUTION/AVAILABILITY OF ABSTRACT <input checked="" type="checkbox"/> UNCLASSIFIED/UNLIMITED <input type="checkbox"/> SAME AS RPT. <input type="checkbox"/> DTIC USERS		21. ABSTRACT SECURITY CLASSIFICATION Unclassified	
22a. NAME OF RESPONSIBLE INDIVIDUAL Dr. Bertram Hui		22b. TELEPHONE (Include Area Code) (202) 394-1264	22c. OFFICE SYMBOL N60921

that total attenuation was expected over most of our measurement range, so the only surprise might be in the extent to which the conductivity exceeds the upper limit of our measurement capability, and thus the predicted values. Simple calculations indicate that the excess ionization we observed could have been caused either by x-ray ionization (from x-rays generated by beam scrape-off upstream of our experimental station) or by a very low current halo surrounding the electron beam core. The latter is the more likely source; such a halo would not be detectable by other diagnostics.

The 10-GHz measurements, located 7 m downstream, measured a conductivity profile that was approximately Gaussian with a 50-cm radius. The absolute conductivity levels were quite low, so that the beam current required to produce them constituted only a small fraction of the total, even when integrated over the large conductivity profile. However, these low conductivities did produce significant attenuation of the 10-GHz probe beam, still exceeding 50% at our largest offset measurement position of 60 cm. These high attenuations at large radii suggest that the multistatic radar beam-tracking scheme proposed by Olsson and Matson at C. S. Draper Laboratory is feasible, but this conclusion is tentative because of uncertainties about the characteristics of the propagating electron beam (i.e., the beam diameter may have been much larger than desired for good propagation and density channel formation).

The conductivity decays following the electron beam pulse were generally faster than expected based on our previous afterglow conductivity decay studies, especially in the case of the 35-GHz measurements in a closed tank at 500 torr and of the 10-GHz open-air measurements. The decay times are in reasonable agreement with calculated electron-attachment times in atmospheric pressure air, but all previous measurements show decay times that are much longer than the calculated attachment times. Rapid conductivity decays would be a problem if conductivity-channel tracking was desired in multiple-pulse beam experiments, but in such experiments the channels would be substantially heated, so that conductivity decays would be expected to be much longer than observed here. Rapid conductivity decays would be advantageous in density-channel tracking studies.

## CONTENTS

<b>LIST OF FIGURES.....</b>	<b>iii</b>
<b>I INTRODUCTION.....</b>	<b>1</b>
Objectives.....	1
Approach.....	3
<b>II BASIC EQUATIONS FOR MICROWAVE DIAGNOSTICS OF PLASMAS.....</b>	<b>5</b>
<b>III EXPERIMENTAL SYSTEMS.....</b>	<b>12</b>
35-GHz Interferometer.....	12
10-GHz Interferometer.....	15
<b>IV RESULTS.....</b>	<b>21</b>
Test Schedule.....	21
35-GHz Closed-Tank Experiments.....	21
35-GHz Open-Tank Experiments.....	25
10-GHz Attenuation Experiments.....	25
10-GHz Interferometer Experiments.....	28
<b>V DISCUSSION.....</b>	<b>32</b>
Attenuation Measurements.....	32
35-GHz Measurements.....	32
10-GHz Measurements.....	34
Conductivity Decay Times.....	35
<b>VI CONCLUSIONS.....</b>	<b>37</b>
<b>ACKNOWLEDGMENTS.....</b>	<b>39</b>
<b>REFERENCES.....</b>	<b>40</b>

Accession For	
NTIS GRA&I	
DTIC TAB	
Unannounced	
Justification	
By	
Distribution/	
Availability Codes	
Dist	Avail and/or Special
A-1	

## LIST OF FIGURES

Figure 1. Schematic of radar tracking technique as proposed by Olsson.

Figure 2. Conductivity profile measurement cell for 35-GHz interferometer.

Figure 3. Tunnel layout for 35-GHz conductivity profile experiments.

Figure 4. Layout of 10-GHz conductivity profile measurement setup at 7 meters propagation distance

Figure 5. Instrumentation for 10-GHz attenuation measurements.

Figure 6. Instrumentation for 10-GHz interferometer measurements.

Figure 7. Representative 35-GHz interferometer signals and reduced data at  $y = +1.5$  cm.

Figure 8. Representative 35-GHz interferometer signals and reduced data at  $y = +12$  cm.

Figure 9. Representative 10-GHz attenuation data at  $y = 0$ , 30, and 60 cm.

Figure 10. Peak line-integrated power attenuation coefficients at 10-GHz versus  $y$ .

Figure 11. Gaussian Abel-inverted peak field attenuation coefficient at 10 GHz versus radius.

Figure 12. Representative 10-GHz interferometer signals and reduced data at  $y = 0$ .

Figure 13. Conductivity profile for the ATA beam predicted by Fawley.

## I. INTRODUCTION

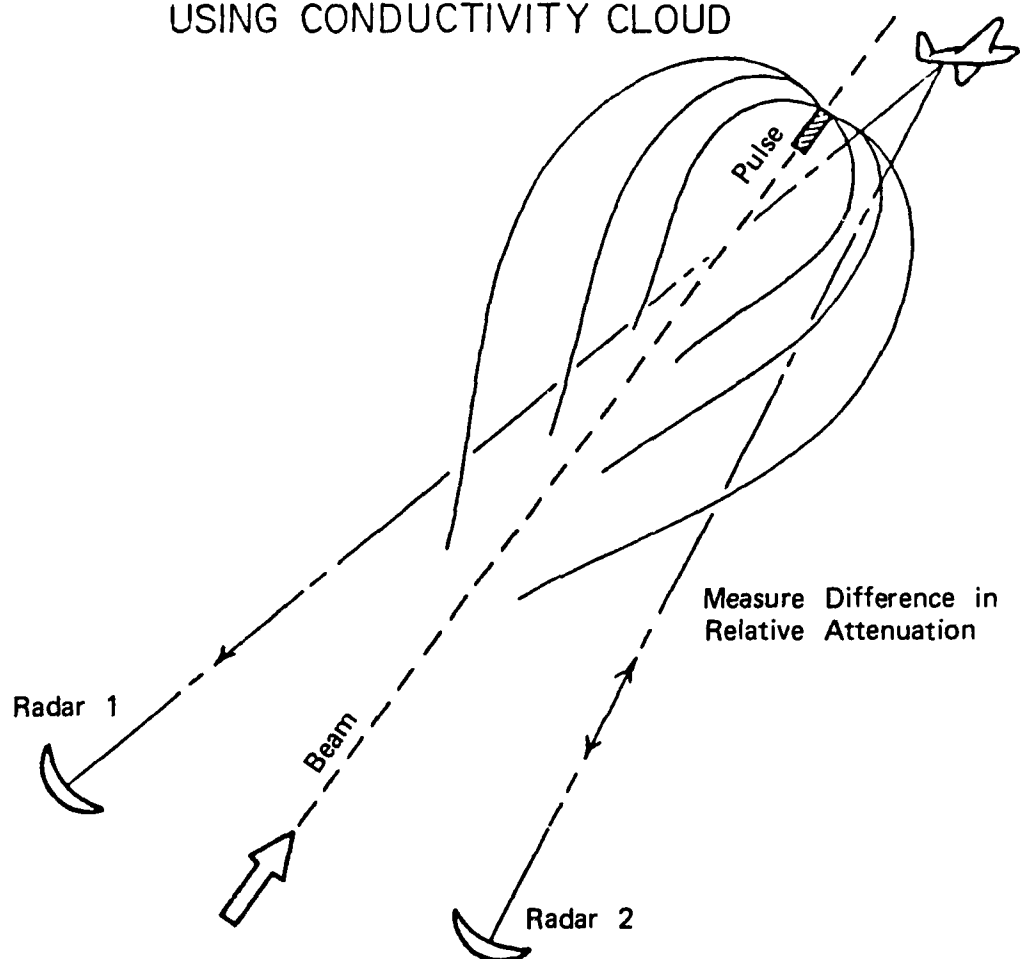
### Objectives

One challenge of developing a charged-particle-beam weapon system is to achieve a means of tracking the propagating beam so as to aid in directing the beam to its target. After considering various alternatives, E. Olsson and L. Matson of C. S. Draper Laboratory [0184, M085] proposed that beam tracking could be carried out using a bistatic radar system as shown in Figure 1. This technique involves monitoring the attenuation by the conductivity cloud surrounding the propagating beam of a radar signal reflected off the target and detected by two or more receivers. The viability of the technique depends on the extent of the surrounding conductivity cloud, which had been calculated but never measured. The principal objective of this program was to measure the extent of the conductivity cloud around propagating beams using microwave absorption and interferometry techniques and to use the results of such measurements to evaluate the proposed beam tracking technique. In this effort, SRI International was responsible for the measurements, and C. S. Draper Laboratory, working under subcontract, was responsible for the subsequent evaluation.

In addition to its importance in evaluating beam tracking, the conductivity profile surrounding the beam is of fundamental importance in studying the beam propagation stability, since the stability is intimately related to return-current distributions, which are governed by the conductivity profile in and around the beam.

The microwave techniques used in these measurements are essentially the same ones required to measure afterglow conductivity decays following termination of the electron beam pulse. Afterglow conductivity measurements are of interest in evaluating channel tracking issues pertinent to multiple pulse propagation. That is, if the second or later pulse in a train is to track the preceding pulse on the basis of a conductivity channel tracking mechanism, optimum tracking is predicted theoretically to occur when the conductivity is  $\sigma_{DC} \approx 5 \times 10^9 \text{ sec}^{-1}$ . For density channel tracking mechanisms,

MULTI-STATIC RADAR SYSTEM  
USING CONDUCTIVITY CLOUD



8112M367-9

EO 10-84



JA-330583-376

Figure 1. Schematic of radar tracking technique proposed by Olsson  
(from [Ol84] with permission).

on the other hand, it is only important that  $\sigma < 5 \times 10^9 \text{ sec}^{-1}$  so as to avoid expulsion of the beam from the channel (so-called channel overheat). In either case, it is important to measure the conductivity decay to determine the optimum pulse spacing in the case of conductivity channel tracking or the minimum pulse spacing in the case of density channel tracking. We have measured afterglow conductivity decays for a number of beams that do not significantly heat the air channel [SDE85a, EDS85, SDE85b], but this program offered the first opportunity to perform measurements where the channel might be hot. Therefore, a second objective was to extend our microwave measurements to include the afterglow conductivity decays.

#### Approach

The basic measurements in the experimental phase of the program consisted of microwave attenuation measurements made transverse to the direction of propagation of an electron beam as a function of radial offset from the beam centerline. Such measurements directly represent the radar tracking technique, although the microwave and radar frequencies might be different (the microwave frequencies were chosen for these experiments to optimize sensitivity to the expected conductivity levels around the channels). When possible, we also performed microwave interferometer measurements, which allow determination of real and imaginary conductivities, and therefore electron densities and collision frequencies. These fundamental plasma properties of the channels then allow calculation of attenuation and refraction by the channel for arbitrary radar frequencies.

We were prepared to perform these measurements in conjunction with any propagating electron beam experiments, but in fact our only opportunity was during the Spring 1987 test series conducted at the Advanced Test Accelerator at Lawrence Livermore National Laboratory. Two separate microwave experimental systems were used in these investigations. The first diagnostic consisted of a 35-GHz interferometer located in the air propagation tank just before the beam dump on Airline 1. Measurements from this apparatus were taken during two phases of the experiment; first, when the beam was not propagated beyond the beam dump (so the test tank was closed and the air pressure controlled), and second, when the electron beam was allowed to propagate in open air beyond the end of the accelerator building.

The second experiment, which consisted of a 10-GHz microwave attenuation system located on the pad area 7 m downstream of the end of the propagation tank, was used only during the open-air propagation phase of the experiment. The primary goal of the outdoor 10-GHz tests was to measure the microwave attenuation coefficient for the off-axis conductivity cloud. After completion of the original task, the system was converted into an interferometer and some conductivity measurements were made.

This report is divided into four parts. First is a review of the basic equations as they pertain to these experiments, second is a description of the experimental apparatus, third is a presentation of the experimental results, and last are the conclusions drawn from the measurements.

## II. BASIC EQUATIONS FOR MICROWAVE DIAGNOSTICS OF PLASMAS

The interactions of electromagnetic waves with a plasma have been described in many references, including the definitive book by Heald and Wharton [HW65]. Here, we present a brief review of the equations relevant to this study.

The plasma is a dielectric medium that affects a propagating electromagnetic wave in three principal ways. First, the waves propagate in plasmas with different wavelengths than in free space. This difference is manifested as a phase change of the wave at a measurement point downstream of the plasma. Second, the waves may be attenuated owing to collisions of wave-induced oscillating plasma electrons with other species in the gas. Third, under some conditions the waves may be reflected rather than transmitted if the wave frequency does not exceed the electron plasma frequency, which is a function of the plasma density. Diagnostic techniques that make use of these properties have been employed for many measurements of plasma phenomena. In these investigations, we made measurements principally of the attenuation, but in the interferometer measurements we also determined the phase shifts.

The space and time dependence of the electric field of the propagating wave is described in complex notation as

$$\begin{aligned} E &= E_0 \operatorname{Re} \exp[j\omega t - j\hat{k}z] \\ &= E_0 \operatorname{Re} \exp[j\omega t - \hat{\gamma}z] \\ &= E_0 \operatorname{Re} \exp[j\omega t - j\hat{\mu}(w/c)z] \end{aligned} \tag{1}$$

Here, the electric field amplitude,  $E_0$ , and the wave angular frequency,  $\omega$ , are taken as real quantities, while the wave number,  $\hat{k}$ , the propagation coefficient,  $\hat{\gamma}$ , and the refractive index,  $\hat{\mu}$ , may in general be complex and defined as

$$\hat{k} = k_r + jk_i,$$

$$\hat{\gamma} = \alpha + j\beta,$$

$$\hat{\mu} = \mu - jx \quad (2)$$

$\alpha$  is called the attenuation coefficient,  $\beta$  is the phase coefficient,  $\mu$  is the refractive index, and  $x$  is the attenuation index. We see that  $\hat{k} = -j\hat{\gamma}$ , so that  $k_r = \beta$  and  $k_i = -\alpha$ . Furthermore,  $\hat{\mu} = -j\hat{\gamma}c/\omega$ , so that  $\alpha = x\omega/c$  and  $\beta = \mu\omega/c$ .

The real part of  $\hat{k}$  or the imaginary part of  $\hat{\gamma}$  are related to the wavelength,  $\lambda$  (and thus to the measured phase change) by

$$k_r = \beta = 2\pi/\lambda \quad (3)$$

Likewise,  $\mu$  is related to the wavelength through the phase velocity of the wave.  $k_i$ ,  $\alpha$ , and  $x$  describe the attenuation of the wave.

The propagation characteristics can be related to the dielectric constant,  $\kappa$ , and the conductivity of the plasma,  $\sigma$ . The dielectric constant is the ratio of permittivities of a plasma to vacuum,

$$\kappa = \epsilon/\epsilon_0 \quad (4)$$

while the scalar conductivity is

$$\vec{J} = \sigma \vec{E} \quad (5)$$

These two parameters can be combined to form a complex dielectric constant as

$$\hat{\kappa} = \kappa_r - j\kappa_i = \kappa - j\sigma/\omega\epsilon_0 \quad (6)$$

or a complex conductivity as

$$\hat{\sigma} = \sigma_r + j\sigma_i = \sigma + j\omega(\kappa - 1)\epsilon_0 \quad (7)$$

Comparison shows that

$$\hat{\kappa} = \kappa_r - jk_i = 1 - j\hat{\sigma}/\epsilon_0\omega = (1 + \sigma_i/\epsilon_0\omega) - j\sigma_r/\epsilon_0\omega \quad (8)$$

and

$$\hat{\sigma} = \sigma_r + j\sigma_i = j\epsilon_0\omega(\hat{\kappa} - 1) = \kappa_i\epsilon_0\omega + j(\kappa_r - 1)\epsilon_0\omega \quad (9)$$

The dispersion relation, which relates the wavelength to the wave frequency, can be written for the different forms of the propagation constants as

$$\begin{aligned} \hat{\kappa}c/\omega &= -j\hat{\gamma}c/\omega = \hat{\mu} = \hat{\kappa}^{1/2} \\ &= (1 - j\hat{\sigma}/\epsilon_0\omega)^{1/2} \end{aligned} \quad (10)$$

Solving for the real and imaginary components of this equation yields

$$\begin{Bmatrix} \kappa_r c/\omega \\ -\kappa_i c/\omega \end{Bmatrix} = \begin{Bmatrix} \beta c/\omega \\ \alpha c/\omega \end{Bmatrix} = \begin{Bmatrix} \mu \\ \chi \end{Bmatrix} = \frac{1}{\sqrt{2}} \left\{ \pm \left[ 1 + \frac{\sigma_i}{\epsilon_0\omega} \right] + \left[ \left( 1 + \frac{\sigma_i}{\epsilon_0\omega} \right)^2 + \left( \frac{\sigma_r}{\epsilon_0\omega} \right)^2 \right]^{1/2} \right\}^{1/2} \quad (11)$$

The upper parameter within each bracket on the left-hand side of the equation corresponds to the plus sign for the first term within the brackets on the right-hand side, while the lower parameter corresponds to the minus sign.

The complex conductivity is related to the electron momentum transfer collision frequency,  $\nu(\nu)$ , and the electron velocity distribution function,  $f_o(v)$ , by the expression

$$\hat{\sigma} = -\frac{4\pi}{3} \frac{n_e e^2}{m} \int_0^\infty \frac{1}{\nu + j\omega} \frac{df_o(v)}{dv} v^3 dv \quad (12)$$

where  $e$  and  $m$  are the charge and mass of the electron. This expression can be evaluated for arbitrary microwave frequency and variation of  $\nu$  with  $v$  if the electron velocity distribution is known. Usually, the distribution is assumed to be Maxwellian, in which case the real and imaginary conductivities can be

calculated as a function of  $T_e$  for arbitrary  $\omega$  and gas pressure. If one further assumes that  $\nu$  is constant, the conductivity can be written simply as

$$\hat{\sigma} = \epsilon_0 \omega_p^2 / (\nu_e + j\omega) \quad (13)$$

or

$$\sigma_r = \epsilon_0 \omega_p^2 \nu_e / (\omega^2 + \nu_e^2) \quad (14)$$

and

$$\sigma_i = -\epsilon_0 \omega_p^2 \omega / (\omega^2 + \nu_e^2) \quad (15)$$

where  $\omega_p^2 = e^2 n_e / \epsilon_0 m_e$  is the square of the electron plasma frequency, which is a function of the plasma density,  $n_e$ , and  $\nu_e$  is now an effective electron collision frequency that is a function of electron temperature.

These expressions show that  $\sigma_r$  is always positive in a plasma, while  $\sigma_i$  is always negative. Careful inspection of equation (6) then shows that an electromagnetic wave travels faster in a plasma than in free space ( $\mu < 1$ ), so that the wavelength is longer. Furthermore, the wave is attenuated in proportion to the magnitude of  $\sigma_r$ .

Our interferometers were fitted with two detectors to measure the power transmitted through the plasma leg,  $P_t$ , and the interference power,  $P_i$ . The latter power is a function of  $P_t$  and the power passing through a reference leg that bypasses the plasma,  $P_r$ , and the phases of the two beams,  $\phi_t$  and  $\phi_r$ , according to the relation

$$P_i = P_t + P_r + 2(P_t P_r)^{1/2} \cos(\phi_t - \phi_r) \quad (16)$$

This equation can be rewritten to yield an expression for the phase change

$$\Delta\phi = \cos^{-1} \left\{ \frac{P_i(t) - P_t(t) - P_r}{2[P_t(t)P_r]^{1/2}} \right\} \quad (17)$$

This phase shift in radians is related to the phase shift in "fringes,"  $\Delta S$ , simply as  $\Delta S = \Delta\phi/2\pi$ . The fringe shift arises from the difference in the number of wavelengths that fit within the plasma pathlength,  $L$ , given by

$$\Delta S = L/\lambda_0 - L/\lambda$$

$$= (\mu_0 - \mu) L/\lambda_0 \quad (18)$$

Since  $\mu_0 = 1$ ,

$$\mu = 1 - \Delta S \lambda/L \quad (19)$$

The field attenuation parameters in the various notations are determined from the transmitted power as

$$-k_i = \alpha = \chi\omega/c = (1/2L) \ln [P_t(t=0)/P_t(t)] \quad (20)$$

where  $P_t(t=0)$  signifies the transmitted power in the absence of a plasma.

In practice, measurement of  $P_t(t)$  and  $P_i(t)$  during a pulse, together with determination of  $P_r$  and  $\phi_t - \phi_r$  before the pulse, allow calculation of  $\alpha(t)$  and  $\Delta\phi(t)$  from equations (20) and (17). We can then determine  $\mu(t)$  and  $\chi(t)$ . From equation (11) we can show that the real and imaginary conductivities are

$$\sigma_r = (2\mu\chi) \epsilon_0\omega \quad (21)$$

and

$$\sigma_i = (\mu^2 - \chi^2 - 1) \epsilon_0\omega \quad (22)$$

Finally, we can calculate  $n_e(t)$  and  $\nu(t)$  from  $\sigma_r$  and  $\sigma_i$  using equation (12). If we use the constant collision frequency approximation, this is done using equations (14) and (15).

When the wave frequency is much larger than the plasma frequency and the collision frequency, the electron density can be determined directly from the measured phase shift by noting that

$$\mu \approx (1 - \omega_p^2/\omega^2)^{1/2}$$

$$\approx 1 - 1/2 \omega_p^2/\omega^2 \quad (23)$$

Then

$$\Delta\phi \approx (2\pi L/\lambda) (\omega_p^2/\omega^2)$$

$$\approx n_e r_e \lambda L \quad (24)$$

The last expression relates  $\omega_p$  to  $n_e$  and compresses atomic constants into the classical electron radius,  $r_e = e^2/m_e c^2 = 2.8 \times 10^{-13}$  cm.

Although the above equations have been written assuming that the plasma properties are uniform according to a "slab" model, in fact, the microwave probe measurements are line integral measurements along the path of the probe beam of properties that typically are not uniform. The paths are designed to be chords transverse to the electron-beam-induced plasma, which is assumed to be cylindrically symmetric. These chordwise integral measurements as a function of radial offset can be converted to local plasma properties as a function of radius by performing an Abel inversion [Bo61, Ba62] if sufficient data along different chords are obtained.

A particularly useful expression results if the integrated quantities vary as a Gaussian. For example, if the total phase shift is given as

$$\Delta\Phi(y) = 2\lambda_0 r_e \int_{-\infty}^{\infty} n_e dx$$

$$= 2\lambda_0 r_e \int_y^{\infty} n_e(r) r dr / (r^2 - y^2)^{1/2} \quad (25)$$

and if  $n_e = n_{e_0} \exp(-r^2/r_0^2)$ , one can show analytically that

$$\Delta\Phi(y) = (\sqrt{\pi}) \lambda_0 r_e r_0 n_{e_0} \exp(-y^2/r_0^2) \quad (26)$$

Thus, the Abel inversion of a Gaussian distribution also is Gaussian. If the line integrated phase shift,  $\Delta\Phi$ , varies as a Gaussian function of  $y$ , a measurement of its  $1/e$  radius ( $r_0$ ) determines the peak density  $n_{e_0}$  as well as

the variation of  $n_e$  with radius. We apply such a Gaussian Abel inversion to the 10-GHz attenuation measurements.

It should be noted that the conductivities quoted in this report are AC conductivities at the microwave probe frequencies used. Conductivities relevant to electron beam propagation are DC values, where

$$\sigma_{DC} = \epsilon_0 w_p^2 / \nu \quad (27)$$

These DC values must be calculated from this equation once the values of  $w_p$  and  $\nu$  have been determined as outlined above.

### III. EXPERIMENTAL SYSTEMS

#### 35-GHz Interferometer

The 35-GHz interferometer horns were located in the propagation tank at the 45.91-m point in Airline 1. The setup is shown schematically in Figures 2 and 3. The homemade rectangular 20-dB gain horns were spaced by 30 cm and were fitted with parallel-plate (venetian blind) lenses designed to focus the microwave probe beam at the midpoint. The horns were mounted on a plate connected to a remotely actuated positioner (LLNL linear probe) through a Wilson seal vacuum feedthrough. The y range of motion of the horns (y is the vertical distance of the center of the horn with respect to the beam centerline) of -4 to +12 cm was made possible by mounting the plate in a short section of eccentric cell as shown in Figure 2. This arrangement allowed measurements nearly as far off-center as the propagation tank inner wall at  $y = 15$  cm. The horn position was controlled by a motor controller located either in the diagnostics lab ("pentagon room") for the in-tank measurements or in the diagnostics bunker when the beam was allowed to propagate in open air. The horns were coupled by flexible waveguides connected to waveguide feedthroughs mounted in the cell wall. Microwave-transmitting vacuum windows separated the flexible waveguide inside the high vacuum propagation tank from the external waveguide constituting the transmit and receive legs of the interferometer. The latter waveguide was WR-28 type, which is standard for  $k_a$  band (26-40 GHz) use, but transitions to WR-90 waveguide (X-band) were made for transmission through the 12-foot-thick concrete floor in order to minimize waveguide attenuation. The waveguide sections from the microwave source to the vacuum window were evacuated by a small mechanical pump to eliminate the possibility of ionization within the waveguide by x-rays generated by the electron beam.

The 35-GHz source and the interferometer mixing and detection components were located in the diagnostics lab located directly above the beamline. The source was a pulsed magnetron borrowed from LLNL's ELF facility; it was capable of delivering 100 kW in a 500-ns pulse. The output waveform was not flat but rather had a ripple amplitude of approximately 10%. Output power from the magnetron was split into two parts, with -20 dB going to the horns

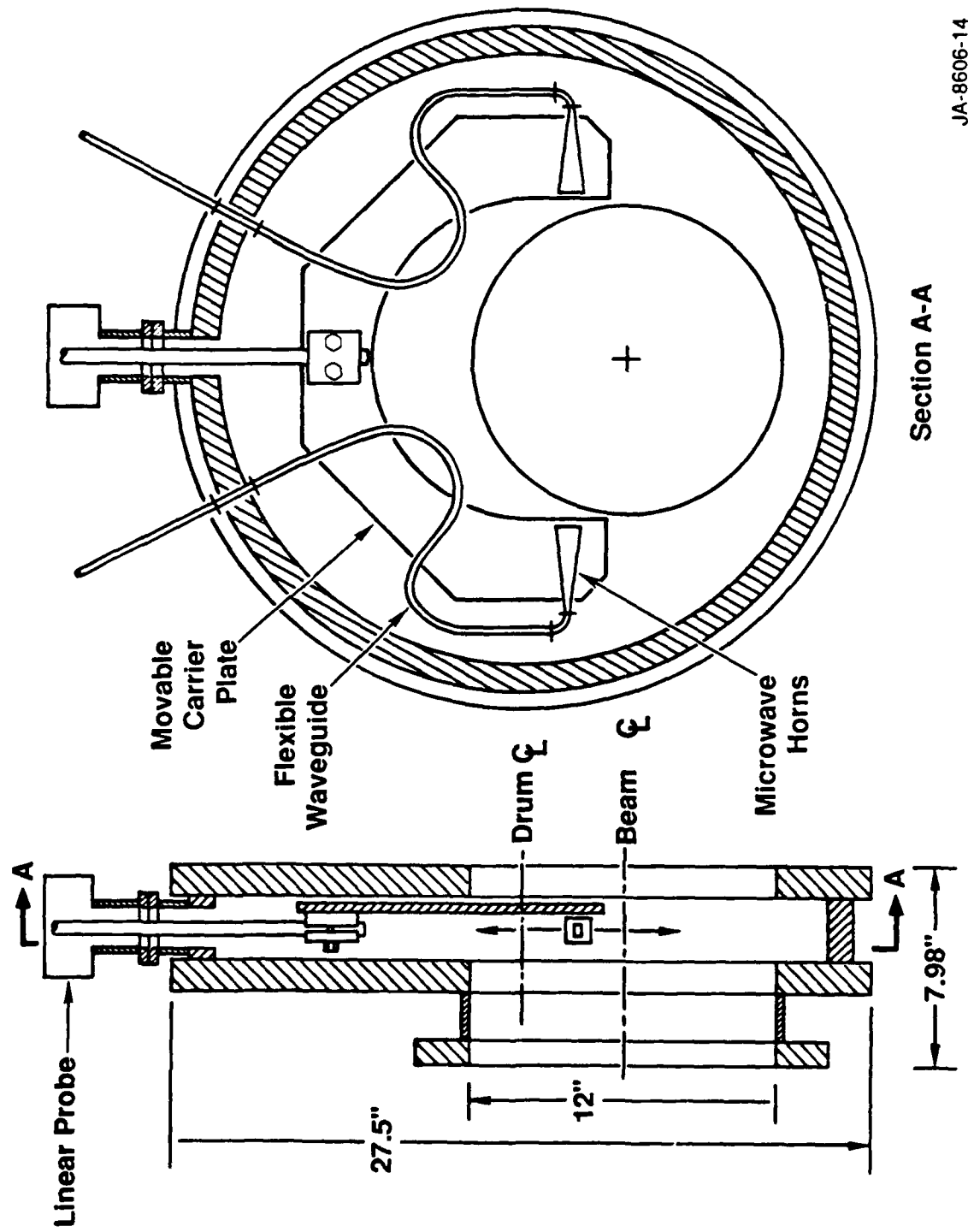
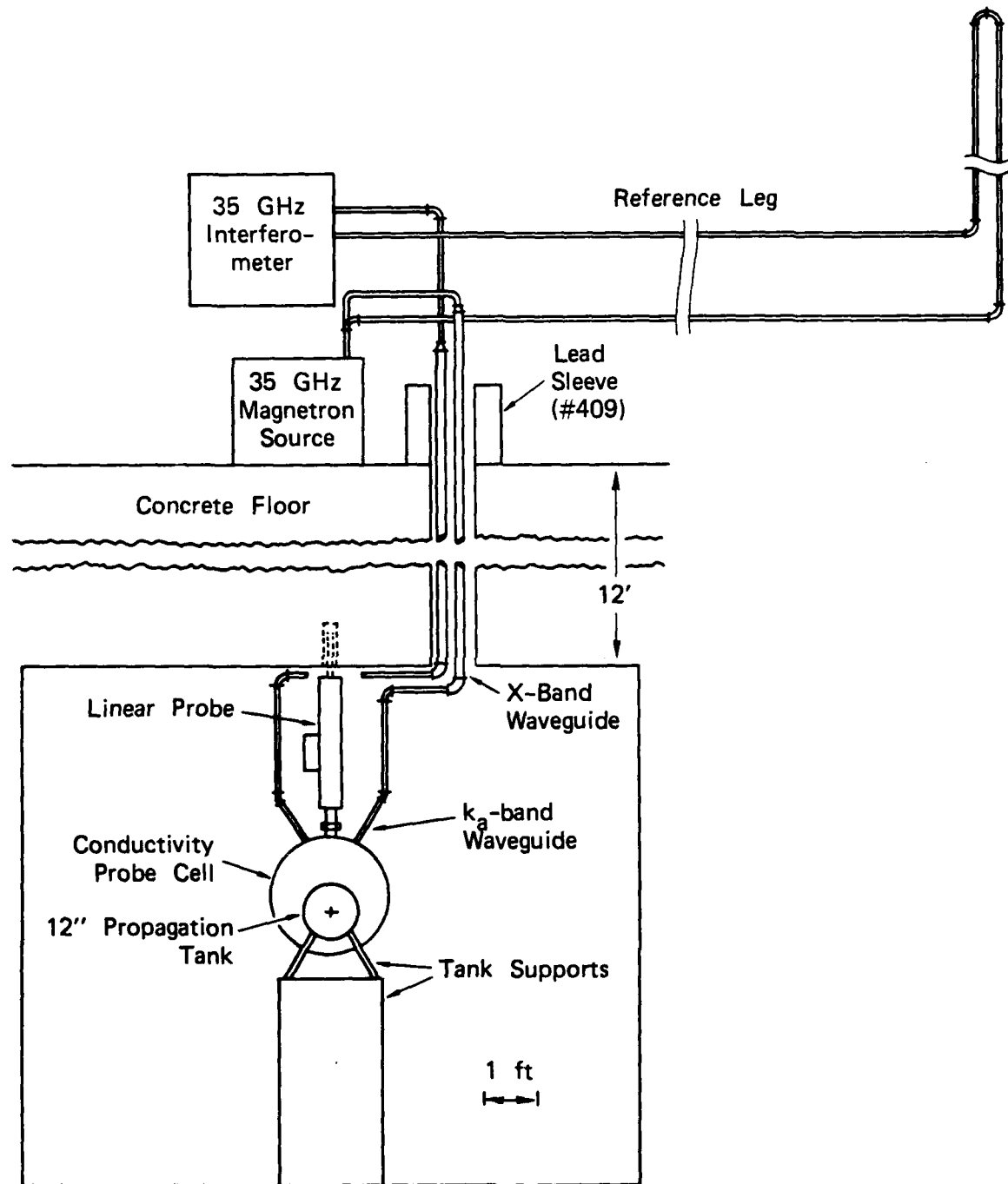


Figure 2. Conductivity profile measurement cell for 35-GHz interferometer.

JA-8606-14

**Section A-A**



JA-8606-13A

Figure 3. Tunnel layout for 35-GHz conductivity profile experiments.

and reference legs and the remainder dumped into a dummy load. A directional coupler split -10 dB of the utilized power to form a reference leg. The remainder went to the interferometer horns. The reference leg was about 20 m long, approximately the same length as the transmit leg in order to equalize time delays in the two legs. This equalization was necessary to synchronize the power fluctuations in the transmitted and reference powers. The detection system was located inside a metal box for electromagnetic noise suppression. The system consisted of two crystal detectors, one to measure the interference signal between the transmit and reference legs and the second to measure the transmitted power directly. 250-MHz-bandwidth amplifiers with 5-dB gain were used to amplify each crystal's output signal. They had 50-ohm input and output impedances, which matched the impedances of the cables and transient digitizers. The electrical output signals from the amplifiers were routed to the diagnostics bunker, where Tektronix 7912AD transient digitizers recorded the signals. An attenuator and phase shifter were placed in the reference leg, and an attenuator was inserted into the transmit leg. Before a series of shots, waveguide electromechanical switches were used to alternately open and close each leg, which permitted the signals to be equalized and the relative phase angles set. In the absence of a plasma, the phase difference was usually adjusted to quadrature ( $\phi_t - \phi_r = 90^\circ$ ), which maximizes the sensitivity of the system. The detectors were calibrated separately using a thermistor power meter, and the resulting voltage versus power curve for each detector was used to convert the signals to transmitted and reference powers.

#### 10-GHz Interferometer

The 10-GHz interferometer horns were located on the pad area, approximately 7 m from the exit foil of Airline 1. An axial view of the 10-GHz system is shown in Figure 4. Plywood support structures were constructed to mount the horns and positioning systems. 20-dB standard gain horns were mounted on plastic plates, which were constrained to move vertically in plastic guides. The E-plane of the horns was vertical and the H-plane was parallel to the beam propagation direction. The horn size limited the spatial resolution to about 6 cm. Positioning was accomplished by a compressed air pneumatic system, that included a control panel placed in the outer area of the diagnostics bunker and 24 plastic tubes running between the bunker and the positioners. The pneumatic system was chosen to eliminate any electrical

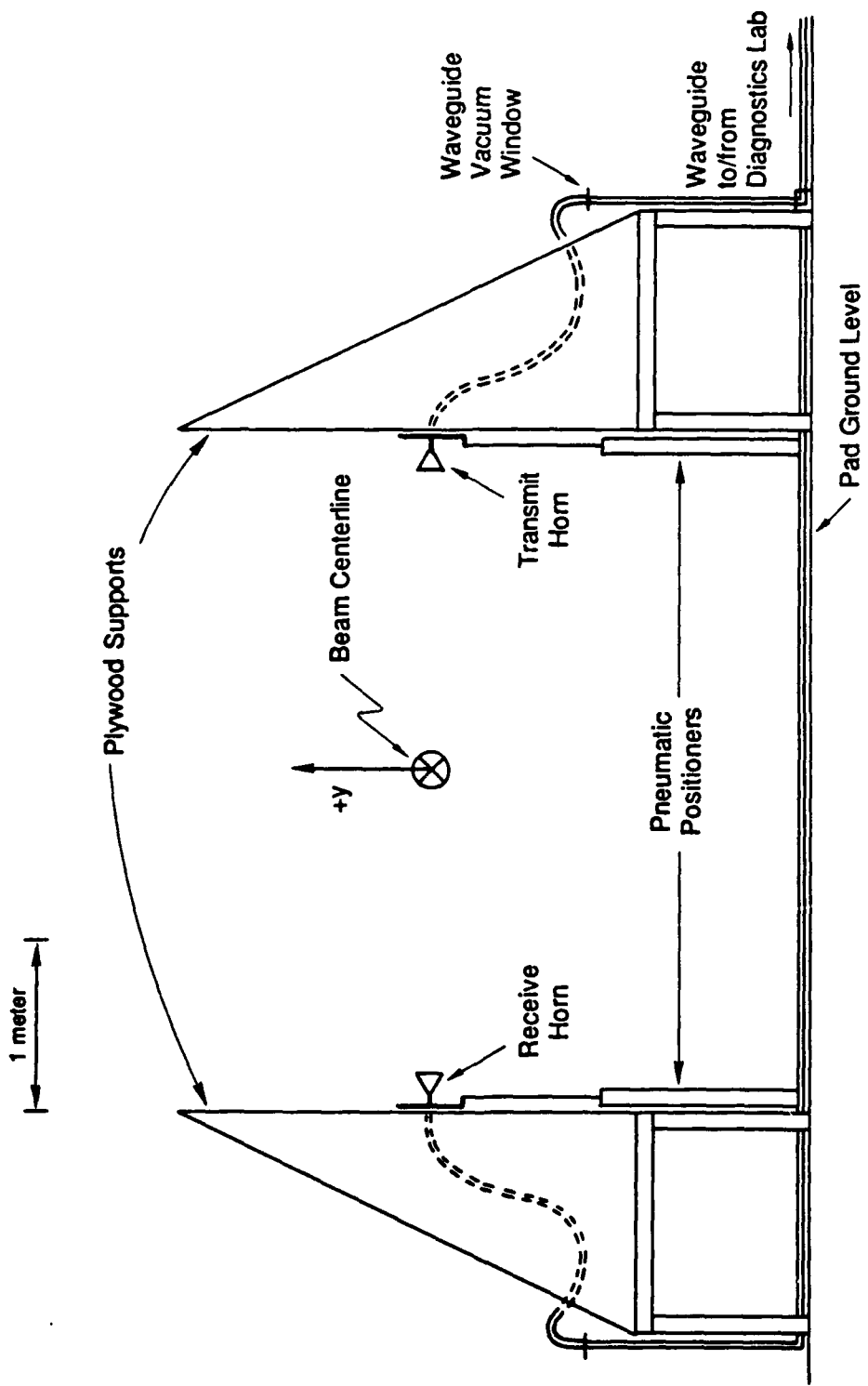


Figure 4. Layout of 10-GHz conductivity profile measurement setup at 7 meters propagation distance.

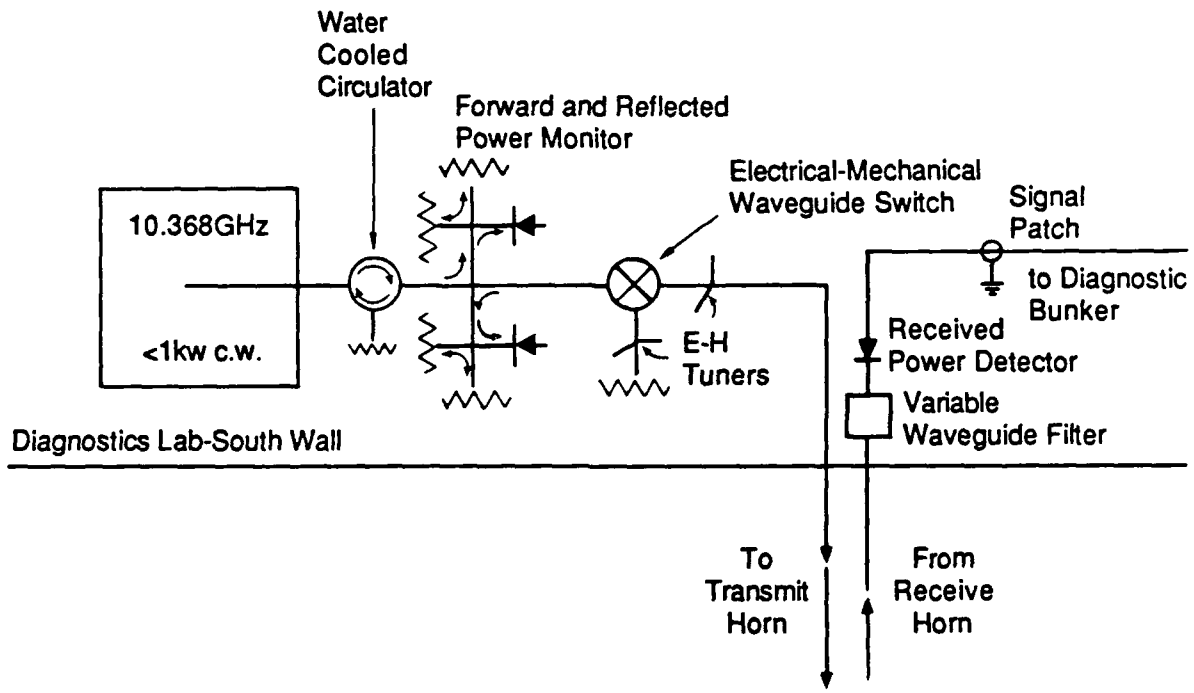
JA-8606-15

components which might be subject to severe EMP conditions and to minimize the amount of metal in the beam propagation area that could affect other electromagnetic measurements. The system only allowed for discrete positioning of the horns at 10-cm intervals. The vertical motion ranged from -50 to + 60 cm with respect to the beam centerline. The horizontal separation of the horns was 4 m, with the beam centerline located approximately midway between the transmit and receive horns. There was approximately 30 dB of insertion loss at this horn separation.

The microwave source, an old X-band radar source, was borrowed from Lawrence Berkeley Laboratory. It consisted of a klystron amplifier driven by a low power klystron oscillator. The output power was set by controlling the input power to the amplifier with a biased PIN diode modulator. The source was capable of delivering approximately 1 kW cw power at the tuned frequency of 10.368 GHz. Typical source power levels for these experiments were in the 100- to 200-watt range. The source was located in the diagnostics lab next to the 35-GHz source. The oscillator klystron power supply was located in a metal box for electromagnetic noise suppression. A flexible metal bellows containing the necessary power and control cables connected the metal box to the source cabinet, which was also an rf-tight metal box.

Output microwave power from the source as well as the received signal power were routed by WR-90 waveguides to feedthroughs in the wall of the building. Outside, the waveguides ran under a catwalk, then down the wall to the ground level of the pad area and across the pad to the bases of the horn stands. The waveguides were connected to the horns by flexible waveguides, and vacuum windows were placed at the interfaces between the rigid and flexible waveguides. The small mechanical pump located in the diagnostics room also evacuated the X-band waveguides in the region between the building feedthroughs and the flexible waveguides; again, this was intended to prevent x-ray-induced ionization in the waveguides from affecting the measurements.

Two detection setups were used. The first, designed solely to measure attenuation of the microwave beam by the plasma, is shown schematically in Figure 5. The received power detector was located in the diagnostics lab, just inside the wall. A narrow-band waveguide filter before the detector was used to block beam-generated microwave noise. Electrical signals, including ATA-supplied beam bug current signals, were patched to the diagnostics bunker



JA-8606-16

Figure 5. Instrumentation for 10-GHz attenuation measurements.

for recording on transient digitizers and storage on the ATA-supplied data acquisition system. After sufficient data had been collected from that experimental arrangement, an interferometer mixing and detection system shown schematically in Figure 6 was built in the diagnostics bunker. A reference leg was run directly to this area. The transmitted power leg also was routed to the area, and the two legs were combined as shown in the figure. The data were again recorded on transient digitizers and were analyzed by the same methods used to analyze the 35-GHz interferometer data.

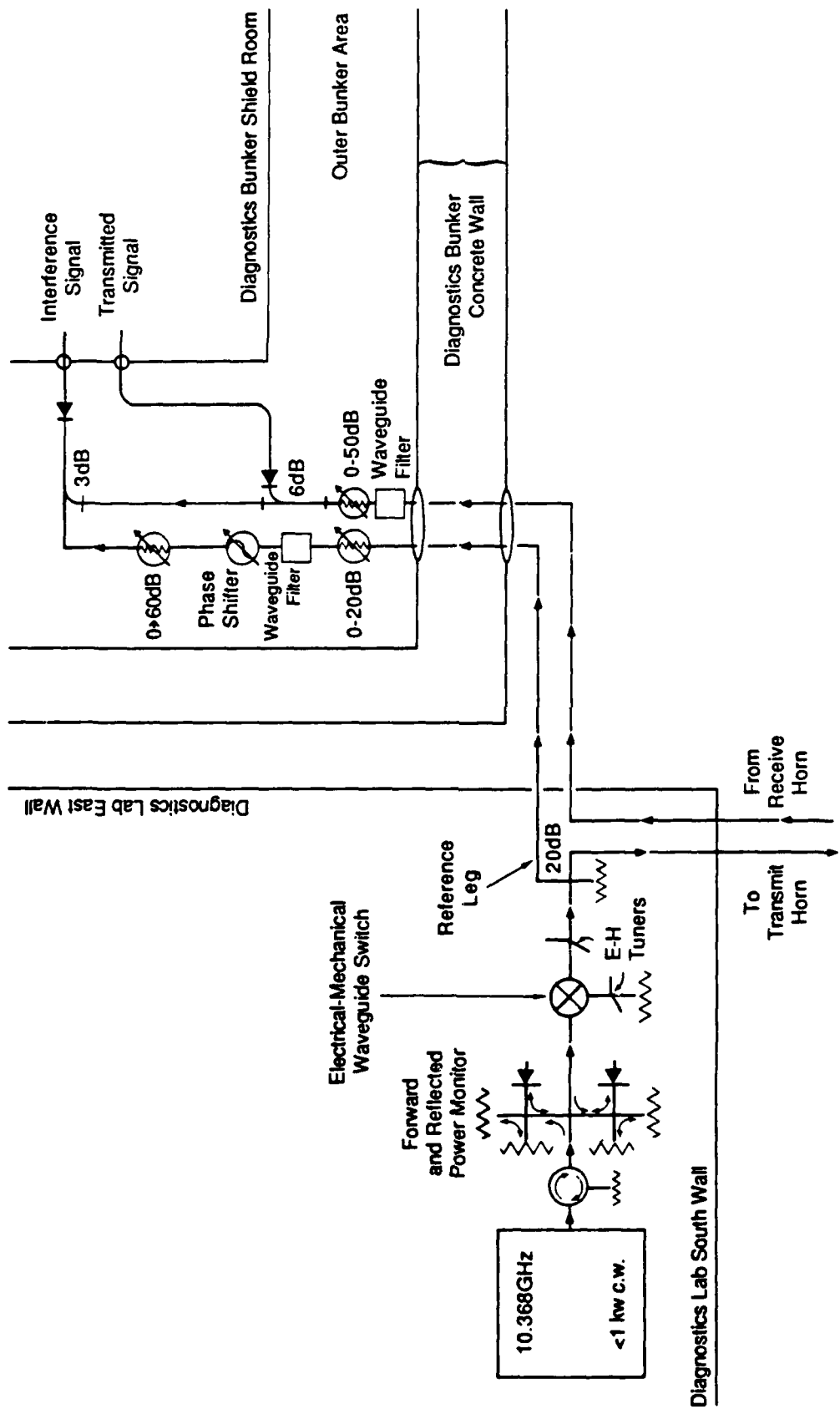


Figure 6. Instrumentation for 10-GHz interferometer measurements.

#### IV. RESULTS

##### Test Schedule

The data were acquired over the course of seven weeks. Table 1 lists the run days when each SRI diagnostic system was used.

##### 35-GHz Closed-Tank Experiments

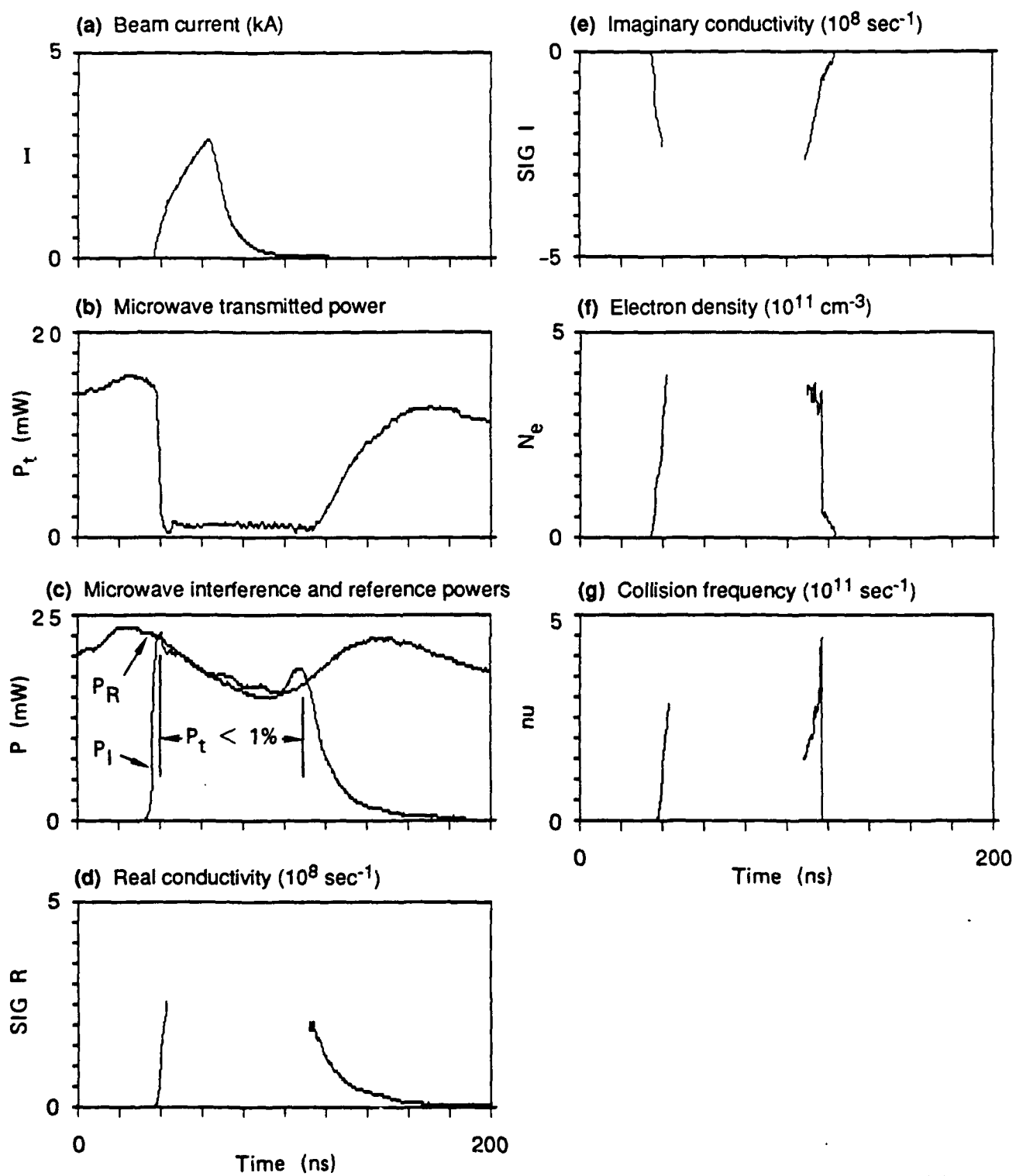
Initial experiments were carried out with the beam stopped in a beam dump at the end of Airline 1, just beyond the location of the 35-GHz interferometer test station. The propagation tank was usually set to a pressure of 500 torr, although on one occasion several experiments were carried out at different pressures. Dry compressed air was used as the fill gas. The data were taken at different y-values corresponding to different radial offsets from the beam centerline. Representative data for the beam bug measured current, transmitted power, interference power, and reference power, and corresponding conductivities, electron densities and collision frequencies calculated from the data are shown for  $y = +1.5$  cm and  $y = +12$  cm in Figures 7 and 8. The data were analyzed according to the equations presented in Section II. These shots were taken with the initial phase angle set to 180 degrees instead of the quadrature condition of 90 degrees. The interference power then is zero prior to the pulse. It appears that the 35-GHz signals were almost entirely attenuated during the electron beam pulse [the exact transmitted power near zero is difficult to determine from Figures 7(b) and 8(b) because of small shifts in the transient digitizer ground level during the pulse], but the transmitted power recovered to the initial value in only approximately 50 ns. A more accurate assessment of the transmitted power near zero can be made by noting that the interference power was equal to the reference power for a portion of time as shown in Figures 7(c) and 8(c), indicating that the transmitted microwave beam was, in fact, totally attenuated. During this "cutoff period" only a lower bound may be made of the electron density; for 35-GHz microwaves this corresponds to a density  $\sim 3 \times 10^{11} \text{ cm}^{-3}$ , depending on the actual length of the plasma and on the electron temperature.

Table 1  
Data Acquisition Schedule for SRI Diagnostics

<u>Day of Year</u>	<u>35-GHz Interferometer</u>	<u>10-GHz Absorption</u>	<u>10-GHz Interferometer</u>	<u>Optical Emission<sup>a</sup></u>
097	X			
099	X			
100	X			
101	X			
105	X			
106	X			
107	X			
110	X			
111	X			
112	X			
127	X			
128	X			X
132		X		X
133		X		X
147	X	X	X	X
148	X			X
150				X

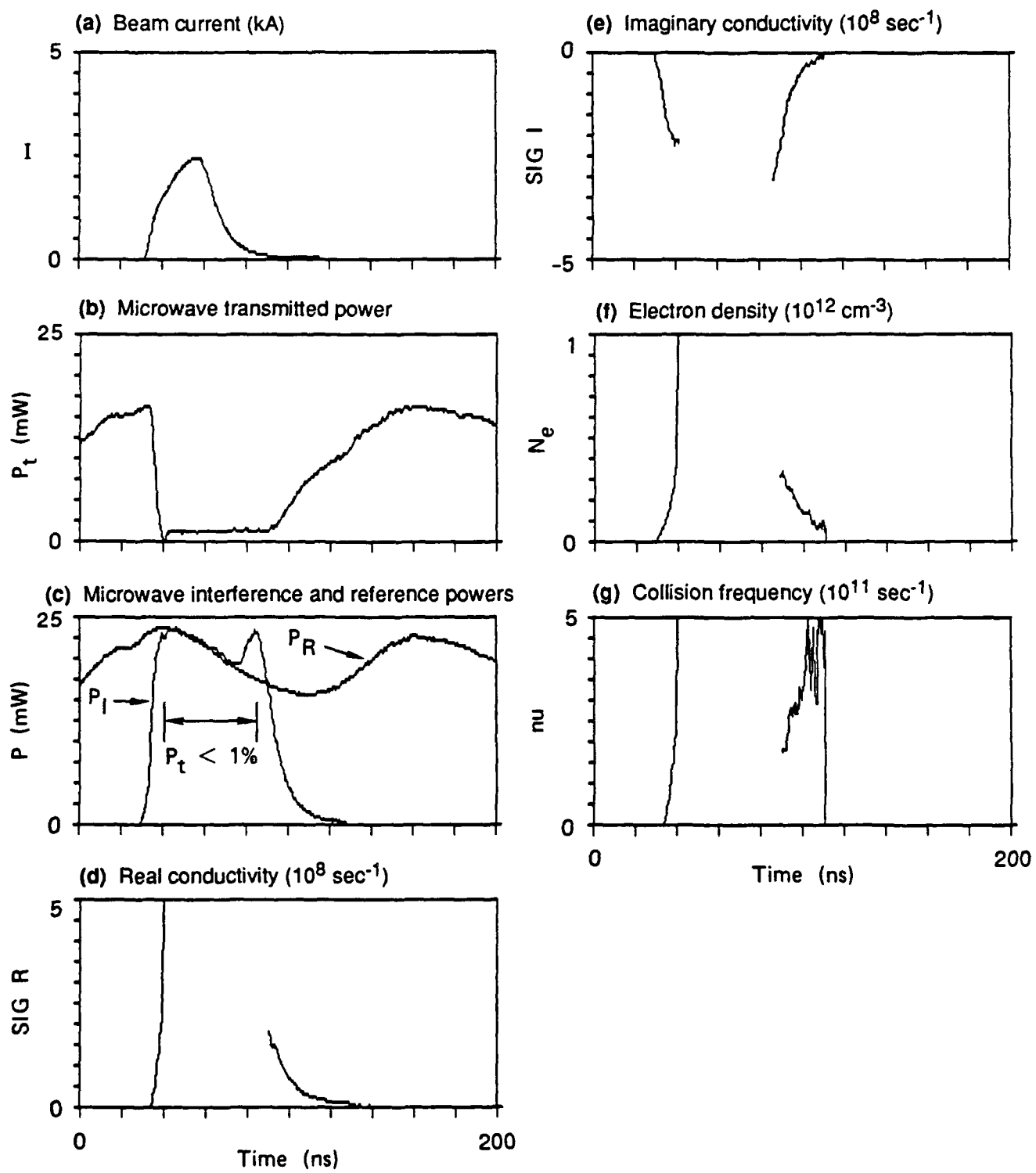
---

<sup>a</sup>Optical emission measurements are discussed in a separate report.



JA-8606-18A

Figure 7. Representative 35-GHz interferometer signals and reduced data at  $y = +1.5 \text{ cm}$ .



JA-8606-19A

Figure 8. Representative 35-GHz interferometer signals and reduced data at  $y = +12 \text{ cm}$ .

The only significant difference in the data for the different  $y$ -values was in the duration of the cutoff period. The electron densities near the beam centerline must have been higher than near the tank wall, and the data indicate that it took longer for the conductivity to decay near the beam centerline, consistent with a higher initial electron density. The peak attenuation in all cases was total, so that no dependence on the  $y$ -position could be determined, and consequently an Abel inversion was impossible. Thus, we were constrained to use the 30-cm path length between the horns to reduce the data to real and imaginary conductivities and then to electron densities and collision frequencies as shown in Figures 7 and 8.

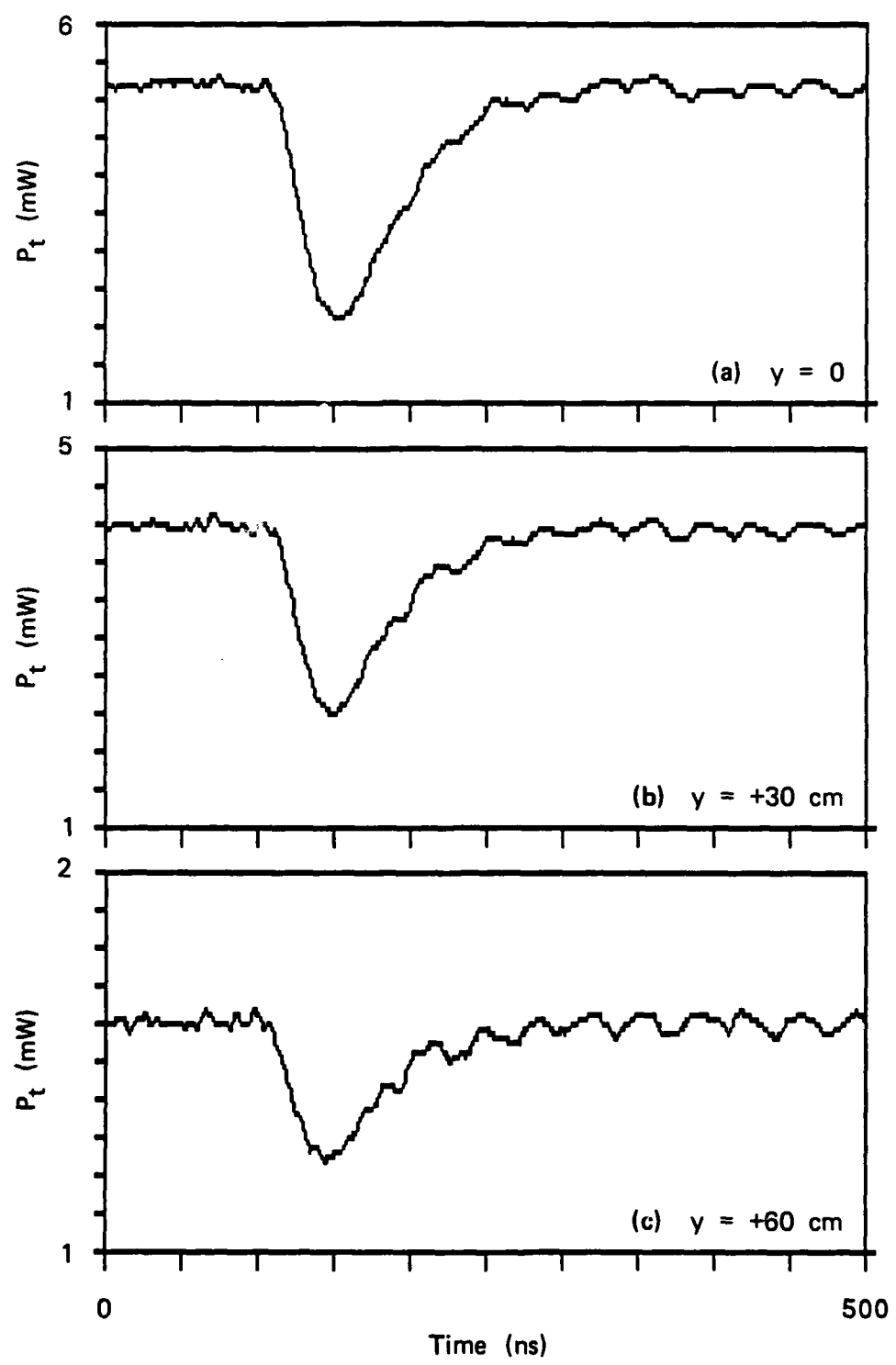
#### 35-GHz Open-Tank Experiments

Data also were collected from the 35-GHz interferometer during the out-the-door phase of the experiments. In those tests, the beam dump was removed and the propagation tank was open to the atmosphere. The results of these experiments were essentially identical to those obtained when the tank was closed, thus confirming the previous conclusions, i.e., that the microwaves were cut off for much of the pulse even at large distances from the beam centerline and that the decay time for the conductivity was less than 50 ns.

#### 10-GHz Attenuation Experiments

Representative time histories of the 10-GHz transmitted power taken at the 7-m station for  $y = 0$ , +30, and +60 cm are shown in Figure 9. Although we subsequently learned of a problem with these measurements (discussed below), we note three surprising features of these results. First, the 10-GHz microwaves were never totally attenuated, even though this lower frequency is sensitive to lower electron densities than the 35-GHz microwaves used in the propagation tank. Second, the attenuation extends to very large radial distances, as exhibited by the 60% power attenuation at 60 cm offset. Third, the apparent plasma lifetime (which should closely track the microwave attenuation) is again very short, with a time constant of less than 100 ns.

Radial attenuation data were collected during several sequences of shots. The results of one sequence are shown in Figure 10, which shows the average values (from up to three shots at each  $y$  location) of the line-integrated peak power attenuation. The largest attenuations, on the beam centerline, were approximately 7 dB, or 80%. The variation of attenuation



JA-8606-20

Figure 9. Representative 10-GHz attenuation data at  $y = 0, 30$ , and  $60$  cm.

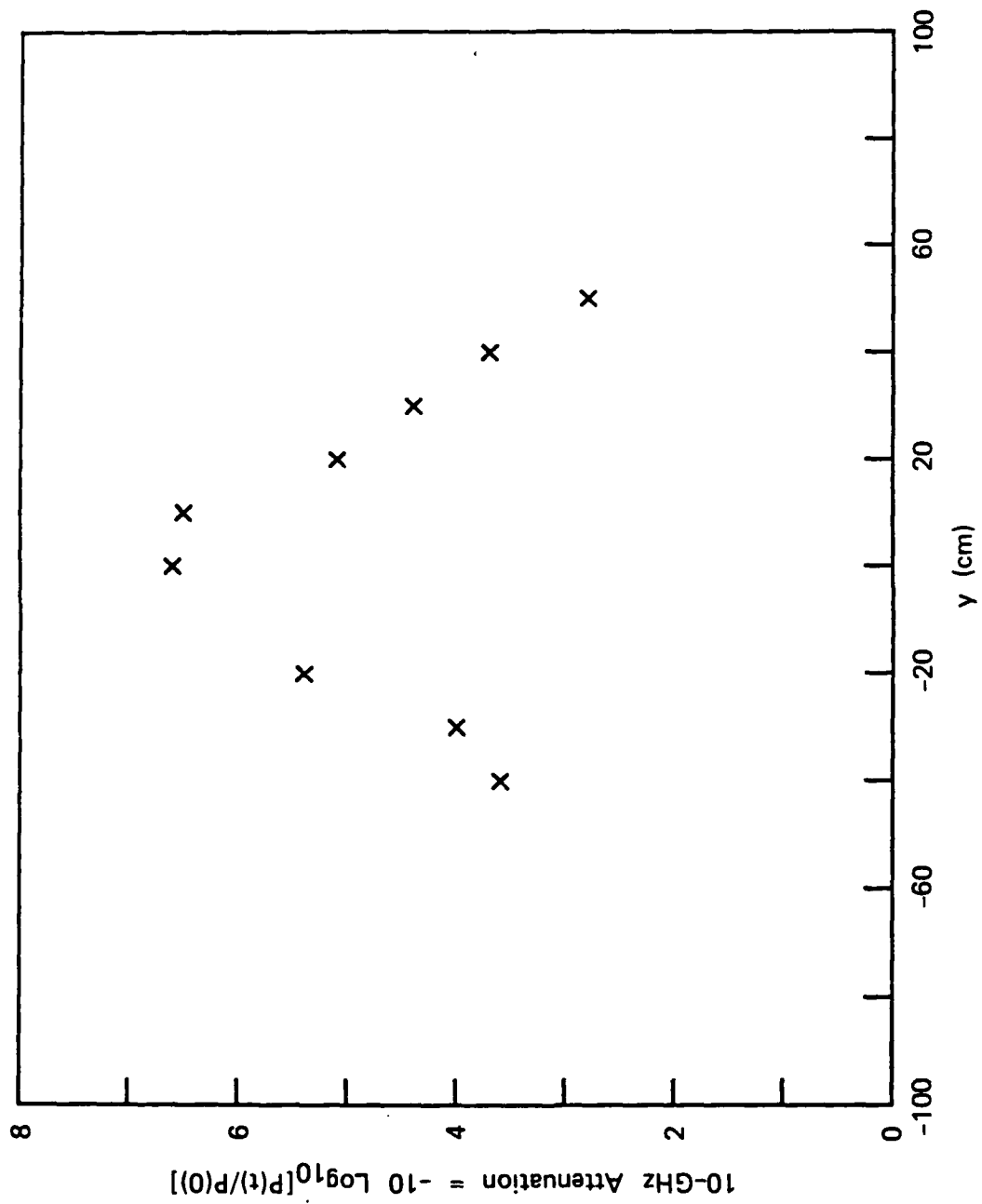


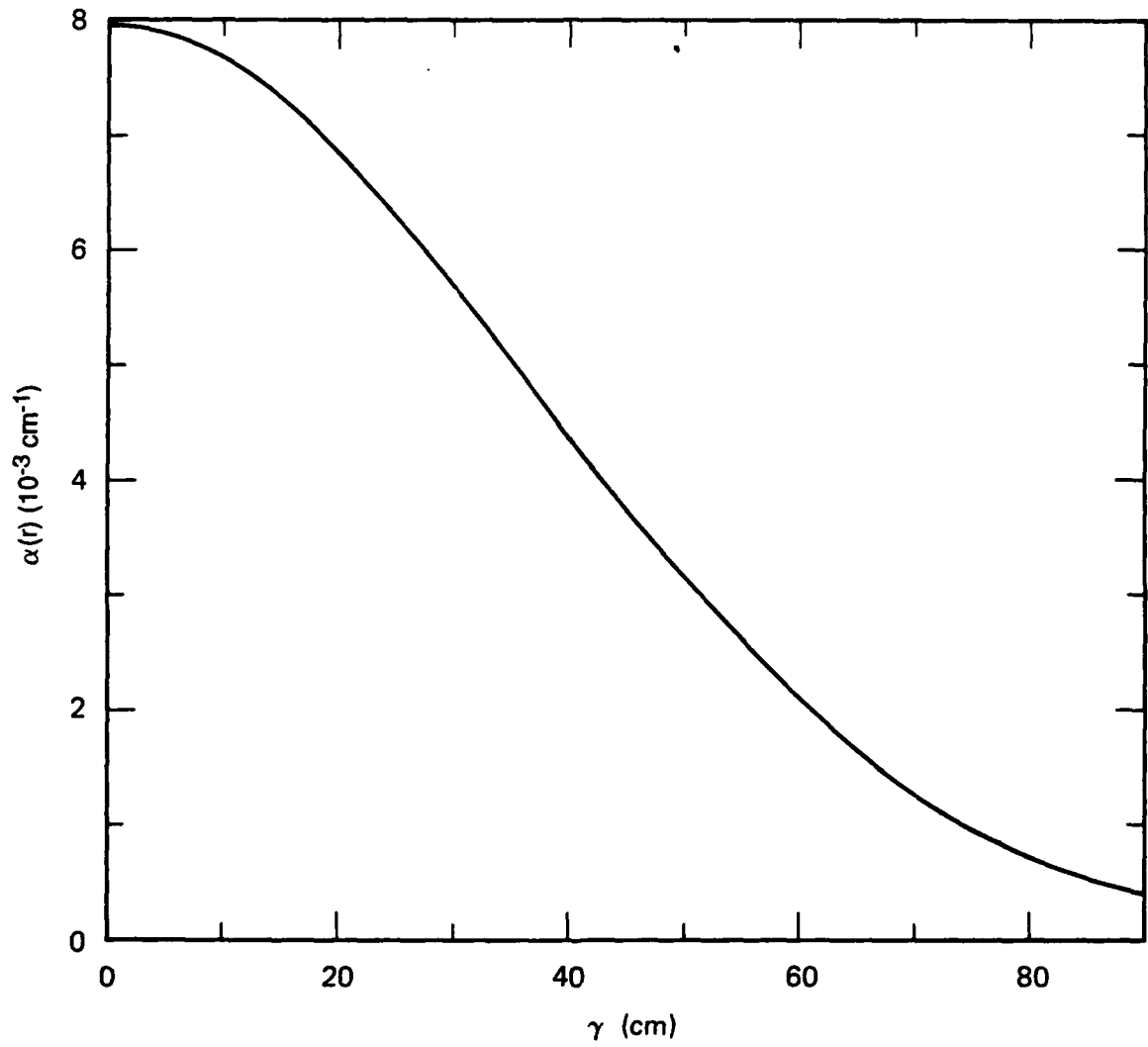
Figure 10. Peak line-integrated power attenuation coefficients at 10-GHz versus  $y$ .

with  $y$  can be well fit to a Gaussian profile with a radius of 52 cm. The analytical Abel inversion for a Gaussian profile, described in Section II, then shows that the peak absorption coefficient on axis was  $8 \times 10^{-3} / \text{cm}$ , decreasing radially with a Gaussian profile as shown in Figure 11.

It appears from the transmitted power histories shown in Figure 9 that the response time of the 10-GHz microwave system was quite long, on the order of 25 ns, and that this slow response masks the true peak attenuation that might occur earlier in the pulse. To investigate the response time, we performed a separate series of experiments after the ATA program was completed. Very short (3-ns) electron beam pulses from a Febetron 706 were used to generate air conductivity clouds located between two horns, and the 10-GHz system response time was measured as various components were added. We found that the bandpass filters used to eliminate possible ATA beam-generated microwaves from disturbing the measurements have a response time of 10 to 15 ns, which is not surprising since the filters were very narrow band (FWHM - 8 MHz). Unfortunately, this limitation was not identified until after the ATA measurements were completed.

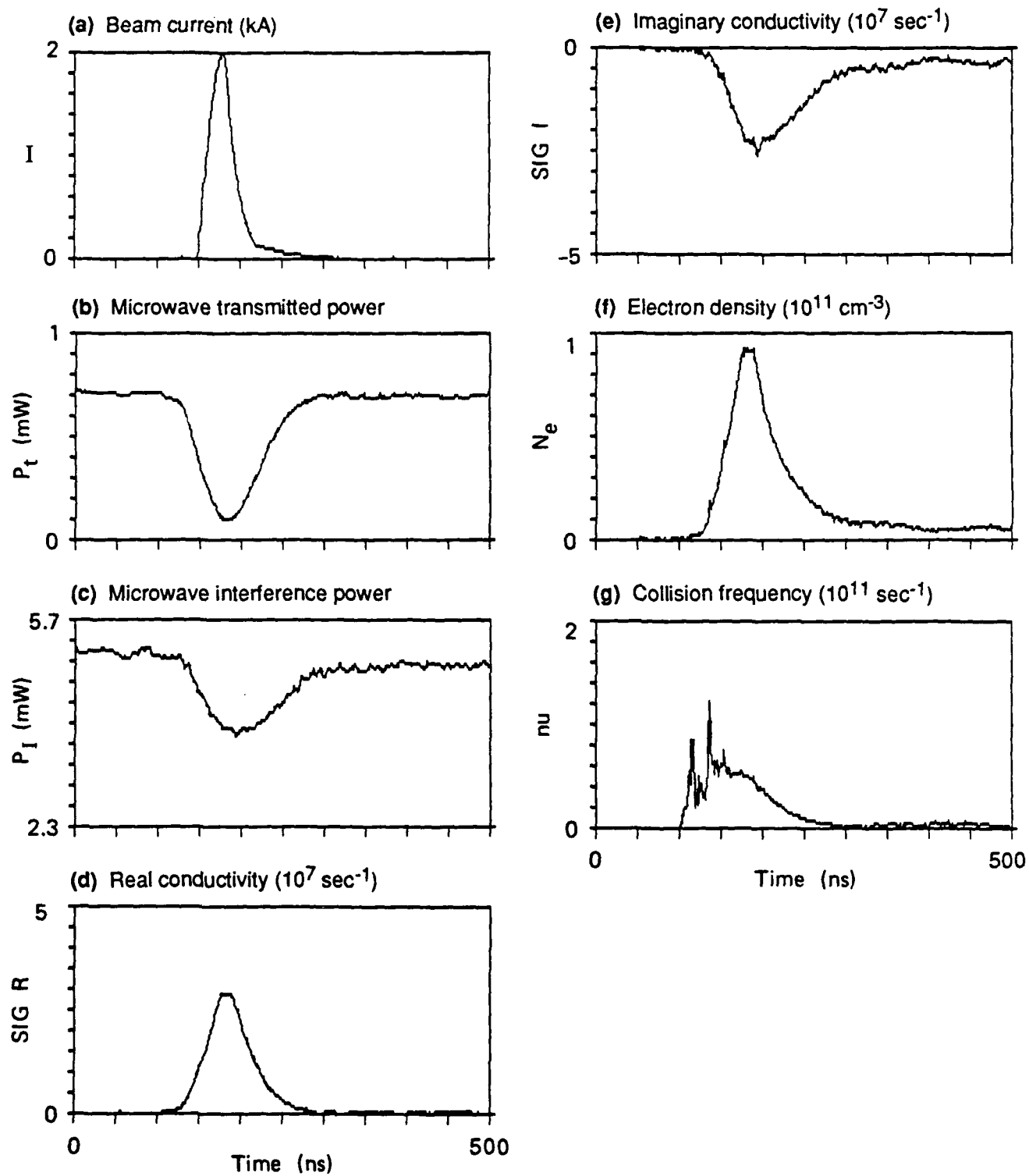
#### 10-GHz Interferometer Experiments

The test schedule was such that we had an opportunity on only one night to make measurements with the 10-GHz system configured as an interferometer. Unfortunately, severe winds that night caused the horn stands to flutter, and the resulting fluctuations in the path length between horns caused corresponding fluctuations in the interference signal in the absence of a plasma. Nevertheless, a set of data was collected for several  $y$ -values. Representative beam-bug-measured current, transmitted and interference powers, and calculated conductivity, electron density, and collision frequency histories for  $r = 0$  are presented in Figure 12. The conductivities, electron densities, and collision frequencies are centerline values calculated using a Gaussian beam radius of 52 cm as determined by the attenuation measurements above. However, the interferometer tests were conducted several days later than the attenuation measurements, so the beam properties may have been different.



JA-8606-22

Figure 11. Gaussian Abel-inverted peak field attenuation coefficient at 10 GHz versus radius.



JA-8606-23A

Figure 12. Representative 10-GHz interferometer signals and reduced data at  $y = 0$ .

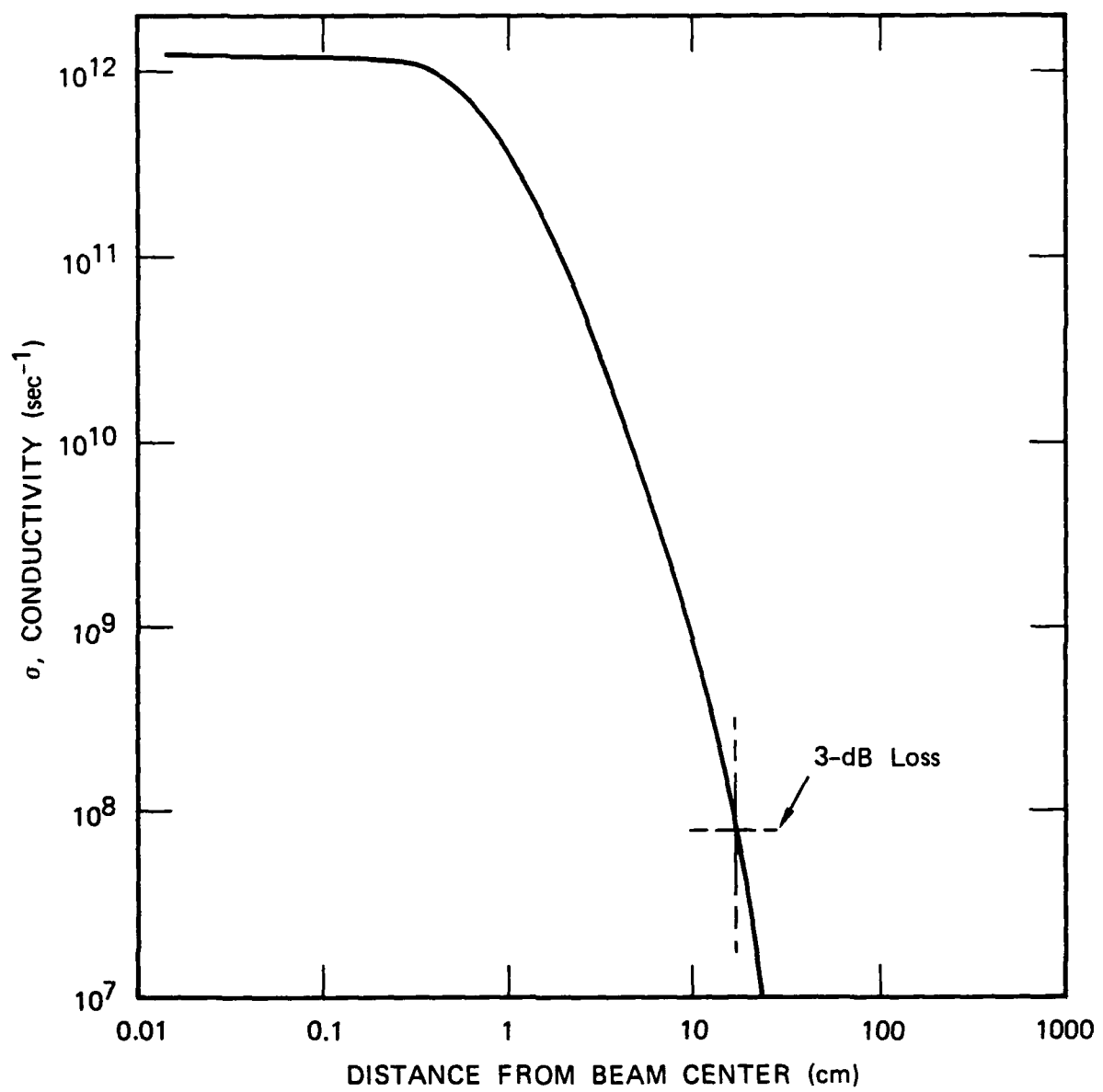
The peak electron densities from Figure 12(f) are  $9 \times 10^{10}/\text{cm}^3$ . These densities can be extrapolated back to the time of the electron beam peak current (to account for the finite response time of the filters) to give peak values of approximately  $3 \times 10^{11}/\text{cm}^3$ . This value is approximately 1/10th the minimum value corresponding to cutoff of the 35-GHz probe beam in the propagation tank. Thus, the electron densities after 7 m of propagation were apparently much lower than at the beginning of the trajectory.

## V. DISCUSSION

### Attenuation Measurements

35-GHz Measurements. The total attenuation of 35-GHz microwaves throughout the propagation tank indicates that electron densities are in excess of approximately  $3 \times 10^{11}/\text{cm}^3$  and microwave conductivities are greater than  $2 \times 10^8 \text{ sec}^{-1}$ . These microwave conductivities correspond to DC conductivities of approximately  $5 \times 10^8 \text{ sec}^{-1}$ , but we expect that the peak conductivities during the electron beam pulse are much higher. We can compare these measured values with predictions by Fawley as shown in Figure 13 (taken from [0184]). The predicted conductivities are above  $10^9 \text{ sec}^{-1}$  as far out as  $r = 10 \text{ cm}$ , and they drop below  $10^8 \text{ sec}^{-1}$  by about 15 cm. Since our quoted values are lower limits, the measured conductivities apparently are somewhat higher (and perhaps much higher) than predicted.

This observation leads us to consider possible sources of ionization that could fill the entire tank cross section. We consider first the possibility of x-ray ionization generated by beam electrons impinging on the tank walls and/or apertures upstream of the test station. The beam loss in the IFR cell directly up-beam from the interferometer horns was reported to be as large as 50% [St87], which constitutes approximately 3 kJ of beam energy. We calculate the conversion efficiency to x-rays to be ~50%, or 1.5 kJ. The absorption cross section for 5 to 50 MeV x-rays in air is about  $0.017 \text{ cm}^2/\text{g}$ . If we assume that the x-ray shower just fills the propagation tank of  $707 \text{ cm}^2$ , then the energy deposition is  $3 \times 10^{-5} \text{ J/cm}^3$ . That much energy deposition would produce a total of  $5 \times 10^{12} \text{ electrons/cm}^3$ , which is more than an order of magnitude more than required to account for the excess ionization. However, there is some question about assigning the excess ionization to x-rays because of an experiment we performed in an attempt to ensure that x-rays propagating outside the propagation tank were not causing problems by generating ionization within the waveguides leading to the tank. In this experiment, we removed the microwave horns from the tank and placed them immediately alongside the tank. We observed no signal in these experiments, indicating a very low level of ionization and consequently a low x-ray flux outside the tank. Since it is unlikely that the x-ray flux would be just confined within



JA-8606-24

Figure 13. Conductivity profile for the ATA beam predicted by Fawley (taken from [O&84]).

the tank, there is reason to doubt that x-rays are responsible for ionization within the tank.

Another possible ionization source throughout the tank is a low-current-density electron beam, i.e., a "halo," around the main central core of the beam, as postulated by Lampe [La87]. The energy deposition required to generate an electron density of  $3 \times 10^{11}/\text{cm}^3$  is  $2 \times 10^{-7} \text{ J/cm}^3$ . This energy deposition requires a current density of approximately  $0.04 \text{ A/cm}^2$ . Integrating this current density over the cross-sectional area of the beamline implies a total current in the halo of approximately 30 A, or less than 1% of the total beam current measured by the beam bugs. The remaining 99% of the beam current could be accounted for in a tight beam, as indicated by LLNL's bow probe measurements, which would not have been detected by the interferometer since the transmitted probe beam was already totally attenuated. Likewise, the bow probe measurements would not have detected a halo of current density  $<0.1 \text{ A/cm}^2$  compared with a peak beam density of  $>1000 \text{ A/cm}^2$ . Therefore, a low-current halo surrounding the main electron beam could also account for the excess ionization we observed, and is, in fact, the most likely source.

10-GHz Measurements. The peak electron densities inferred from these measurements at the 7-m propagation distance were  $9 \times 10^{10}/\text{cm}^3$ , but the peak values were limited by the finite response time of the interferometer. Extrapolation of the electron densities backward in time to the presumed peak in electron density gives a peak on-axis density on the order of  $3 \times 10^{11} \text{ cm}^{-3}$ . This density is the same as the minimum electron density inferred for the wings of the beam in the upstream 35-GHz experiments, and the implied current density for such an electron density is again approximately  $0.04 \text{ A/cm}^2$ . Integrating over a Gaussian electron beam profile of peak density  $0.04 \text{ A/cm}^2$  and radius of 52 cm accounts for approximately 500 A, which is only about 10% of the beam current presumably propagating in air. Thus, we draw three conclusions from these measurements.

(1) The ionization levels inferred from the measurements account for only a fraction of the total beam current. Three explanations for this observation are possible. First, our extrapolation of electron densities back to peak values may underestimate the actual peak values; second, our limited spatial resolution may preclude detecting a small, high-current-density beam

on axis; and third, the beam may have expanded so rapidly that most of the current is propagating at extremely low current densities outside the range of our measurements (note that there was still large attenuation at our largest y measurement location of +60 cm). The last possibility is most unlikely, since our optical Faraday cup measurements (to be reported separately) always showed at least 50% of the beam current propagating within the 18-cm field of view of the optical system.

(b) The beam profile in the attenuation measurements consisted of a Gaussian shape with ~50 cm radius. Note that this profile is based on measurements confined to <60-cm radial offset, so that we did not measure the wings of the profile. Thus, we probably cannot distinguish between a Gaussian and a Bennett profile. In either case, the beam detected by the 10-GHz microwave measurements appears to consist of a broad, low-current profile.

(c) The strong attenuation of 10 GHz microwaves at large radii indicates that the multistatic radar tracking scheme proposed by Olsson and Matson should be viable. However, this conclusion must be regarded as tentative because we do not know how the attenuation profiles were affected by the propagation characteristics of the beam, nor do we know how the attenuation profiles would vary with propagation distance. Nevertheless, the existing results are encouraging for the practicality of the tracking technique.

#### Conductivity Decay Times

The conductivity decay times for both the 35- and 10-GHz measurements were very short, with a time constant typically <50 ns for both the 500 Torr air in the propagation tank and the open air cases. The decay times expected depend on the range of conductivity being measured. Our previous measurements of conductivity decays following Febetron excitation of atmospheric pressure air show that  $\sigma_r$  decays to  $10^6 \text{ sec}^{-1}$  by 1  $\mu\text{s}$ ; extrapolation of the measurements to earlier times indicate that a value of  $10^7 \text{ sec}^{-1}$  occurred at approximately 200 ns and  $10^8 \text{ sec}^{-1}$  occurred at approximately 50 ns [SDE85a]. However, the decay rate was strongly pressure dependent, and at 500 torr the time constants should be about twice as long. Thus, in the 35-GHz measurements in the propagation tank at 500 torr, where the conductivity decays from  $2 \times 10^8$  to  $10^7$  in approximately 30 ns [Figure 8(d)], the decay times are shorter than expected by approximately a factor of 4, but the same decay times at full atmospheric pressure would be more nearly consistent with

our previous results. By contrast, the 10-GHz measurements show conductivities decaying from  $3 \times 10^7$  to  $10^6$  in approximately 75 ns [Figure 12(d)], while our previous work indicates a decay time of 1  $\mu$ s.

The conductivity decay times are governed by electron loss processes, which in these experiments consist primarily of electron-ion recombination and electron attachment. In clean air at atmospheric pressure, the electron attachment rate is  $5.5 \times 10^7 \text{ sec}^{-1}$ , which corresponds to a time constant of 18 ns. Thus, attachment could account for the fast decays, although all previously measured decay rates have been more than an order of magnitude slower than the calculated rate. The recombination rate for electrons with  $\text{O}_4^+$  is approximately  $2 \times 10^{-6} [\text{n}_e] \text{ sec}^{-1}$ , where  $[\text{n}_e]$  is the electron density. For  $\text{n}_e = 3 \times 10^{11}/\text{cm}^3$ , typical of the 35-GHz measurement [Figure 8(f)], the rate is  $6 \times 10^5$ , so the time constant is 1.6  $\mu$ s, which is much longer than the observed value. For the 10-GHz measurements,  $\text{n}_e \sim 9 \times 10^{11}$ , so the decay time due to recombination would be even longer, in contrast to the measured value.

The above scaling calculations indicate that electron attachment to  $\text{O}_2$  in air could explain the fast conductivity decay times, although this conclusion conflicts with our previous observations. This apparent discrepancy prompted us to speculate that the gas in the closed propagation tank might be contaminated with high electron affinity trace gases, which would increase the electron attachment rate. These gases might have come from two possible sources. The first is halocarbons trapped in the foam used for microwave absorbing material in the conductivity cell. The second is leaks of high electron affinity gases (e.g.,  $\text{SF}_6$ ) into the propagation tank. To check the first possibility, we removed the Eccosorb foam absorbing material and repeated the experiments; we found no change in the results. The second possibility was eliminated during the open tank phase of the experiments when the same results were observed. Water vapor may have contributed to the fast decay times, but there was no significant difference between the tank experiments using dry air and the open air experiments using humid air.

## V. CONCLUSIONS

The experiments on conductivity profiling around a propagating electron beam planned under this contract were successfully performed during the Spring 1987 series of open-air propagation experiments on ATA at LLNL. Our measurements consisted of both 10- and 35-GHz microwave interferometer measurements of real and imaginary conductivity histories along chords at various  $y$ -offsets from the beam centerline and at two different locations along the propagating beam line. The conclusions of our study are as follows.

The 35-GHz probe beam, located near the beam exit foil at the end of the closed beamline, was totally attenuated during the electron beam pulse, for the total range of the measurements from  $y = -4$  cm to  $y = +12$  cm. Theoretical calculations indicate that total attenuation was expected over most of our measurement range, so the only surprise might be in the extent to which the conductivity exceeds the upper limit of our measurement capability, and thus the predicted values. Simple calculations indicate that the excess ionization we observed could have been caused either by x-ray ionization (from x-rays generated by beam scrape-off upstream of our experimental station) or by a very low current halo surrounding the electron beam core. The latter is the more likely source; such a halo would not be detectable by other diagnostics.

The 10-GHz measurements, located 7 m downstream, measured a conductivity profile that was approximately Gaussian with a 50-cm radius. The absolute conductivity levels were quite low, so that the beam current required to produce them constituted only a small fraction of the total, even when integrated over the large conductivity profile. However, these low conductivities did produce significant attenuation of the 10-GHz probe beam, still exceeding 50% at our largest offset measurement position of 60 cm. These high attenuations at large radii suggest that the multistatic radar beam-tracking scheme proposed by Olsson and Matson at C. S. Draper Laboratory is feasible, but this conclusion is tentative because of uncertainties about the characteristics of the propagating electron beam (i.e., the beam diameter may have been much larger than desired for good propagation and density channel formation).

The conductivity decays following the electron beam pulse were generally faster than expected based on our previous afterglow conductivity decay studies, especially in the case of the 35-GHz measurements in a closed tank at 500 torr and of the 10-GHz open-air measurements. The decay times are in reasonable agreement with calculated electron-attachment times in atmospheric pressure air, but all previous measurements show decay times that are much longer than the calculated attachment times. Rapid conductivity decays would be a problem if conductivity-channel tracking was desired in multiple-pulse beam experiments, but in such experiments the channels would be substantially heated, so that conductivity decays would be expected to be much longer than observed here. Rapid conductivity decays would be advantageous in density-channel tracking studies.

The data presented in this report represent only a small fraction of the total obtained during the course of the experiments. Individual data shots which represent actual beam conditions at a particular time of interest are available for comparison with other diagnostics.

#### ACKNOWLEDGMENTS

We would like to acknowledge the kind hospitality of the entire ATA staff. We greatly benefited from discussions with and from the assistance of Frank Chambers, Bill Fawley, and Chip Smith. Ken Struve deserves special recognition and gratitude for supervising and supporting our activities during the experiment. We would also like to thank Ian Brown and Fred Schlachter of LBL for lending us the X-Band microwave source and various components, and Ted Orzechowski, Al Throop, and Jim Dunlop for lending us the 35-GHz magnetron source and accessories. Finally, we thank Ed Olsson, Les Matson, and John Vytal of C. S. Draper Lab for their support in planning experiments, evaluating microwave propagation issues for the planned experimental arrangements, and assessing the results.

## REFERENCES

[Ba62] W. L. Barr, J. Opt. Soc. Am. 52 885 (1962)

[Bo61] K. Bockasten, J. Opt. Soc. Am. 51 943 (1961)

[Ch87] F. W. Chambers, private communication.

[EDS85] D. J. Eckstrom, J. S. Dickinson, and M. N. Spencer, "Diagnostics Development for E-Beam Excited Air Channels. Conductivity Measurements on the PHERMEX Electron Beam," Technical Report No. 2, Contract N00014-85-C-0718, July 1985.

[HW65] M. A. Heald and C. B. Wharton, Plasma Diagnostics with Microwaves. John Wiley and Sons, Inc., New York, 1965.

[La87] M. Lampe, Proceedings of the SDIO/DARPA/Services Annual Propagation Review, 1987, to be published.

[MO85] L. Matson and E. A. Olsson, Proceedings of the Annual Propagation Physics Review of the Defense Advanced Research Projects Agency and of Army, Navy, Air Force. LLNL Report No. CONF 8506141, p. 315, (1985), [secret].

[O184] E. A. Olsson, presentation at the Fall Coordination Meeting of the Charged Particle Beam Program, Albuquerque, New Mexico, October 1984 (unpublished).

[SDE85a] M. N. Spencer, J. S. Dickinson, and D. J. Eckstrom, "Diagnostics Development for E-Beam Excited Air Channels. Afterglow Conductivity Studies of the Febetron Electron Beam," Technical Report No. 1, Contract N00014-84-C-0718, SRI International, July 1985.

[SDE85b] M. N. Spencer, J. S. Dickinson, and D. J. Eckstrom, "Diagnostics Development for E-Beam Excited Air Channels. Conductivity Measurements on the Medea Electron Beam," Technical Report No. 3, Contract N00014-84-C-0718, SRI International, September 1985.

[St87] K. W. Struve, private communication.